Instability of sheared density interfaces

Eaves, Tom; Balmforth, Neil J.

Published in:
Journal of Fluid Mechanics

DOI:
10.1017/jfm.2018.827

Publication date:
2019

Document Version
Peer reviewed version

Instability of sheared density interfaces

T. S. Eaves† & N. J. Balmforth

Department of Mathematics, University of British Columbia,
1984 Mathematics Road, Vancouver BC, V6T 1Z2, Canada

(Received ?; revised ?; accepted ?. - To be entered by editorial office)

Of the canonical flow instabilities (Kelvin–Helmholtz, Holmboe-wave and Taylor–Caulfield) of stratified shear flow, the Taylor–Caulfield instability (TCI) has received relatively little attention, and forms the focus of the current study. First, a diagnostic of the linear instability dynamics is developed that exploits the net pseudomomentum to distinguish TCI from the other two instabilities for any given flow profile. Second, the nonlinear dynamics of TCI is studied across its range of unstable horizontal wavenumbers and bulk Richardson numbers using numerical simulation. At small bulk Richardson number a cascade of billow structures of sequentially smaller size may form. For large bulk Richardson number, the primary nonlinear traveling waves formed by the linear instability break down via a small-scale, Kelvin–Helmholtz-like roll-up mechanism with an associated large amount of mixing. In all cases, secondary parasitic nonlinear Holmboe waves appear for late times for high Prandtl number. Third, a nonlinear diagnostic is proposed to distinguish between the saturated states of the three canonical instabilities based on their distinctive density-streamfunction and generalised vorticity-streamfunction relations.

Key words:

---

1. Introduction

For geophysical flows at scales much smaller than the Rossby deformation radius, the dynamics is dominated by the interaction and competition between the effects of ambient density stratification and shear. Understanding this dynamics is essential for quantifying the degree of the small-scale mixing that occurs in the oceans and atmosphere, and has motivated a number of observations that have collected vertical profiles of density, horizontal velocity and dissipation or shear production. Ideally, one would like to take such data and predict the subsequent evolution, in addition to inferring what fluid mechanical activity was responsible for the observed state.

Classical analysis of stratified shear flow instability identifies three types of unstable modes that are popularly referred to as Kelvin–Helmholtz (KHI) (Kelvin 1871; Helmholtz 1868), Holmboe-wave (HWI) (Holmboe 1962) and Taylor–Caulfield instability (TCI) (Taylor 1931; Caulfield *et al.* 1995). One descriptor for these modes is in terms of wave interactions: assuming that the flow contains distinctive regions with an interfacial character, KHI is often thought of as resulting from the interaction of waves riding on two vorticity interfaces. HWI arises when the coupled waves are supported by one density and one vorticity interface, whereas TCI owes its origin to the interaction between two density interfaces. For flows in which vertical stratification and shear are the only contributors to the dynamics, these three canonical instabilities exhaust the potential wave interactions and so paint a complete picture of the linear normal mode stability of such flows.

The nonlinear dynamics and mixing properties of KHI have been well studied (Scinocca 1995;

† Email address for correspondence: tse23@math.ubc.ca

Caulfield & Peltier 2000; Peltier & Caulfield 2003; Mashayek & Peltier 2012*a*,*b*; Mashayek *et al.* 2013; Mashayek & Peltier 2013), and HWI has also received recent attention (Smyth & Winters 2003; Smyth *et al.* 2007; Salehipour *et al.* 2016). By contrast, TCI has been explored much less, with its general character and mixing ability yet to be determined. The first two-dimensional computations of TCI by Lee & Caulfield (2001) observed that the density interfaces become drawn together to pinch off the intervening layer and generate distinctive elliptical "Taylor–Caulfield billows." They also observed that in the pinch-off region, a smaller billow sometimes formed whose origin and relation to the primary TCI was unclear. Moreover, the simulations were conducted at relatively small Reynolds number which inevitably subdues many secondary instabilities.

Balmforth *et al.* (2012) also studied the nonlinear dynamics of TCI using a reduced model relevant to long horizontal wavelength and weak stratification; again, billow-like structures emerged from the primary TCI. In addition, the higher Reynolds number of these simulations permitted the observation of secondary instabilities at late times that took the form of parasitic nonlinear Holmboe waves. Such secondary features were confirmed at finite-wavelength by Eaves & Caulfield (2017). However, the saturated states of the primary TCI modes were quite different in the higher bulk Richardson number simulations of that study, resembling propagating, cuspy nonlinear waves rather than billows. Thus, existing studies provide an inadequate characterization of the nonlinear dynamics of TCI, failing to even fully describe the possible structures of the saturation states formed by the primary instability. A key aim of the current work is to conduct numerical simulations of TCI over a wide range of flow parameters in order to properly map out the parameter-dependent, primary and secondary, nonlinear dynamics.

Partly underscoring the fact that relatively little is known about the nonlinear dynamics of TCI is the fact that, unless the Péclet number is sufficiently large ($O(10^5)$), the density interfaces diffuse excessively as the primary TCI grows to finite amplitude. This renders large three-dimensional simulations extremely expensive in terms of grid resolution and time-stepping. Moreover, Eaves & Caulfield (2017) observed a strong dependence of the secondary instabilities on the presence of confining walls, demanding that simulation domains be relatively deep. For these reasons, we conduct two-dimensional simulations to flesh out the nonlinear dynamics of TCI over a wide range of parameter settings, rather than targeting a relatively small number of three-dimensional cases. This limits the realism of our results, but enables us to survey the dynamics and catalogue the parasitic secondary instabilities that limit the lifetime of the primary TCI in two dimensions.

The presence of three types of linear stratified shear flow instability raises the question of how one may diagnose which evolves on a given basic state and then follow on to predict the ensuing nonlinear dynamics. This goal requires a categorisation and classification scheme for the linear and nonlinear behaviour expected for disturbances to a given stratified shear flow. With this in mind, we propose a means to distinguish TCI from KHI and HWI at the linear level for an arbitrary flow profile, and formulate a nonlinear diagnostic to distinguish between their saturated states.

Some previous discussion of techniques for distinguishing KHI from HWI at the linear level has been provided by Carpenter *et al.* (2010) (see also Carpenter *et al.* (2011)). The motivation was to suggest how one might anticipate the subsequent nonlinear flow dynamics and degree of mixing by drawing a convenient distinction between these two linear instabilities, particularly given that KHI is more efficient at mixing and hence 'stronger' than HWI, although HWI is typically longer-lasting (see for example Salehipour *et al.* 2016). The classification of Carpenter *et al.* (2010), however, has some level of arbitrariness and cannot distinguish TCI when the base shear flow has inflection points. We instead consider the net pseudomomentum (Bühler 2014) of a linear normal mode, which can be used to compare the contributions from density or vorticity

interfaces in the evolution of the unstable mode and provides a criteria for deciding whether any given mode has the character of KHI, HWI or TCI. We apply our diagnostic to the flow originally considered by Taylor (1931) for which the distinction between KHI and TCI is ambiguous, and also the flow considered by Holmboe (1962) which exhibits both KHI and HWI and to which Carpenter *et al.* (2010) applied their diagnostic.

For a nonlinear diagnostic, we consider steady nonlinear structures that can be characterized by functional relations between the streamfunction and the density or a generalized vorticity (Long 1953). These relations suggest a means to distinguish between the final states reached after the saturation of the linear instabilities by interrogating the numerical solutions. Since such streamfunction relations do not explicitly depend on spatial position, they may also be obtained from individual vertical profiles such as might be extracted from observations. With this in mind, we examine some oceanographic and laboratory measurements of KHI, HWI and TCI (van Haren *et al.* 2014; Tedford *et al.* 2009; Caulfield *et al.* 1995) to extract approximate streamfunction relations for comparison with our diagnostic.

In section 2 we formulate the stratified shear flow problem mathematically, in section 3 we derive and discuss the linear pseudomomentum conservation law, and in section 4 we describe our suite of nonlinear TCI simulations. In section 5 we show the streamfunction relations contained in the equations of motion and find the relations which represent typical KHI, HWI and TCI saturated states, discuss the use of limited data sets to approximate these relations, and demonstrate the method as applied to the approximated oceanographic and experimental data. We draw our conclusions in section 6.

2. Governing equations

We consider a two-dimensional stratified shear flow in channel with characteristic height H, velocity U, and density difference $\Delta\rho$. Scaling lengths, velocities and density deviations by these quantities (respectively), we arrive at the dimensionless Boussinesq equations, in terms of streamfunction ψ, vorticity ζ, and density ρ:

$$\zeta = \nabla^2\psi, \tag{2.1}$$

$$\rho_t + \{\psi, \rho\} = Pe^{-1}\nabla^2\rho, \tag{2.2}$$

$$\zeta_t + \{\psi, \zeta\} + J\rho_x = Re^{-1}\nabla^2\zeta, \tag{2.3}$$

where the Poisson bracket is given by

$$\{f, g\} \equiv f_x g_y - f_y g_x, \tag{2.4}$$

and the Péclet, Reynolds, bulk Richardson and Prandtl numbers are

$$Pe = \frac{UH}{\kappa}, \quad Re = \frac{UH}{\nu}, \quad J = \frac{\Delta\rho g H}{\rho_0 U^2}, \quad Pr = \frac{\nu}{\kappa}, \tag{2.5}$$

and $\rho_0 \gg \Delta\rho$ is a reference density. Here κ is the diffusivity of the density field (e.g. due to temperature or salinity diffusion), ν is the kinematic viscosity of the fluid medium and g is the gravitational acceleration.

The channel is periodic in the horizontal direction with (dimensionless) length L_x. For our discussion of classical linear stability results in §3, the scales H, U and $\Delta\rho$ represent characteristics of the base equilibrium profiles of flow speed and density, and the shear flow is taken to unbounded in the vertical. In the numerical computations of §4, we consider a finite channel with no normal flow and buoyancy flux through the walls of the channel, which are located at $y = \pm 1$ (the channel having heigth $2H$). We further fix the shear stress rather than the horizontal velocity at $y = \pm 1$ to minimise the effect of the confining walls and avoid viscous boundary layer

instabilities (cf. Eaves & Caulfield 2017). In this situation, we take the initial horizontal velocity and density deviation to be $u = \pm 1$ and $\rho = \mp 1$ at $y = \pm 1$ (so the channel walls are initially moving at a dimensional speed of $2U$ with respect to one another and $2\Delta\rho$ is the initial density difference).

3. Pseudomomentum and linear categorisation

In the wave-interaction interpretation of stratified shear instability, one looks for resonance conditions between waves riding on vorticity and density interfaces. Such conditions by themselves, however, are not sufficient to predict instability; one must further show, based on the conservation laws of the system, that the interaction leads to instability because the waves have opposite sign of energy, momentum or action. Below we establish the pseudomomentum of waves in our stratified shear flows; the arguments also complement the over-reflection arguments of Lindzen & Barker (1985).

3.1. *The pseudomomentum of a linearised disturbance*

The inviscid linearised equations for perturbations $\check{\psi}$, $\check{\zeta}$ and $\check{\rho}$ about the base flow profiles $U(y)$ and $\bar{\rho}(y)$ are

$$\check{\zeta}_t + U\check{\zeta}_x - U''\check{\psi}_x + J\check{\rho}_x = 0 \tag{3.1}$$

$$\check{\rho}_t + U\check{\rho}_x + \bar{\rho}'\check{\psi}_x = 0. \tag{3.2}$$

Formulating the combination

$$\left\langle \left\{ \left[J + \frac{U''(U-c_*)}{\bar{\rho}'} \right] \frac{\check{\rho}}{\bar{\rho}'} \right\} (\text{eq 3.2}) \right\rangle - \left\langle \left[\check{\psi} + \frac{(U-c_*)\check{\rho}}{\bar{\rho}'} \right] (\text{eq 3.1}) \right\rangle, \tag{3.3}$$

where $\langle ... \rangle$ denotes an integral over the area of the spatial domain and c_* is an arbitrary constant velocity, we arrive at a conservation law:

$$\frac{\mathrm{d}\mathcal{E}}{\mathrm{d}t} = 0, \quad \mathcal{E} = \left\langle \tfrac{1}{2}(\check{\psi}_x^2 + \check{\psi}_y^2) + \frac{J\check{\rho}^2}{2\bar{\rho}'} - (U-c_*)U''\frac{\check{\rho}^2}{2\bar{\rho}'^2} - (U-c_*)\frac{\check{\rho}\check{\zeta}}{\bar{\rho}'} \right\rangle \tag{3.4}$$

(cf. (2.28) of Abarbanel *et al.* 1986).

For normal modes, we have $\check{\psi}(x,y,t) = \hat{\psi}(y)e^{ik(x-ct)} + c.c.$, where k is the wavenumber and $c = c_r + ic_i$ is the complex phase speed. We may further exploit the normal-mode equations, $\hat{\zeta} = (U''\hat{\psi} - J\hat{\rho})/(U-c)$ and $\hat{\rho} = -\bar{\rho}'\hat{\psi}/(U-c)$, to arrive at the conserved quantity,

$$M = \frac{\mathcal{E}}{(c_r - c_*)} = \left\langle \tfrac{1}{2}\check{\psi}^2 \left[\frac{U''}{|U-c|^2} + \frac{2J(U-c_r)\bar{\rho}'}{|U-c|^4} \right] \right\rangle = \langle \mathcal{M}_V + \mathcal{M}_B \rangle, \tag{3.5}$$

with

$$\mathcal{M}_V = \tfrac{1}{2}\frac{U''\check{\psi}^2}{|U-c|^2} \qquad \& \qquad \mathcal{M}_B = \frac{J(U-c_r)\bar{\rho}'\check{\psi}^2}{|U-c|^4}. \tag{3.6}$$

The quantity M represents the net pseudomomentum of a linear disturbance; the time rate of change of its density $\mathcal{M}_V + \mathcal{M}_B$ represents the local acceleration of the mean flow induced by the disturbance (Bühler 2014). Moreover, because M is conserved, the exponential growth of any linear perturbation with normal-mode form is forbidden unless $M = 0$ for that mode, as noted originally by Synge (1933) and discussed by Miles (1961) and Howard (1961).

For unstratified flow with $\bar{\rho}' = 0$, the condition $M \equiv \langle \mathcal{M}_V \rangle = 0$ leads to the inflexion-point criterion. With stratification, the fact that the contributions to M must cancel for an unstable normal mode constrains the types of wave interactions that can lead to instability: gravity waves

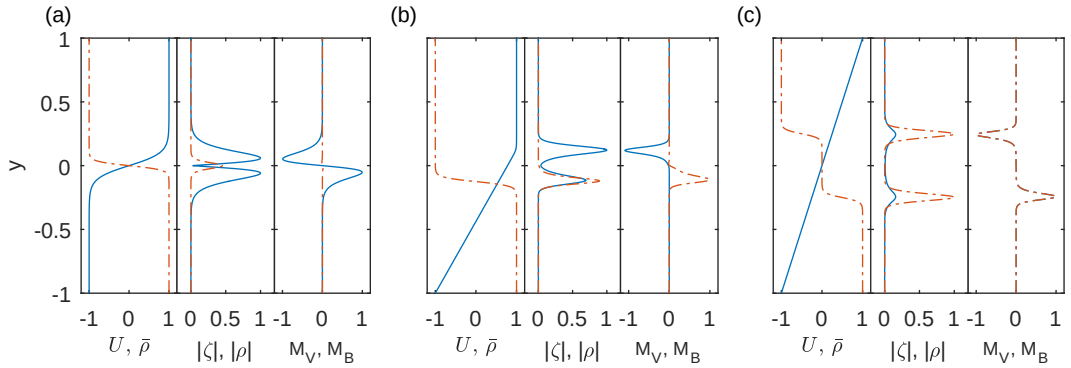

FIGURE 1. Columns from left to right: sample background profiles $U(y)$ (blue solid) and $\bar{\rho}(y)$ (red dot-dashed) for (a): KHI, (b): HWI and (c): TCI. Absolute value of vorticity (blue) and density (red dot-dashed) for the associated growing mode. $\mathcal{M}_V$ (blue solid, when non-zero) and $\mathcal{M}_B$ (red dot-dashed) for the background profiles and the associated modes.

localized at a density interface have a sign for the pseudomomentum density $\mathcal{M}_B$ given by $\mathrm{sgn}(U - c_r)$ (given $\bar{\rho}' < 0$ for stable stratification). Thus, waves riding on two density interfaces with phase speed between the flow speeds of the interfaces have opposite signs of $\mathcal{M}_B$, setting the scene for TCI. In particular, if $U'' = 0$, TCI modes must have cancelling interfacial contributions to the pseudomomentum to give $M \equiv \langle \mathcal{M}_B \rangle = 0$.

Likewise, HWI can only arise when a wave on a density interface, with a pseudomomentum contribution through $\langle \mathcal{M}_B \rangle$, interacts with a wave on a vorticity interface, with an oppositely signed contribution from $\langle \mathcal{M}_V \rangle$. This demands that $U''(U - c_r) > 0$, a Fjortoft-like condition that rules out instability for certain flow profiles that nevertheless allow wave resonances (cf. Carpenter *et al.* 2010). For such stable interfaces, we also see that the criterion $M = 0$ is stronger than the Miles–Howard criterion, as the local Richardson number vanishes throughout the bulk of the flow.

Some examples of the pseudomomentum contributions of unstable modes are shown in figure 1. These modes are computed from the linear eigenvalue problem for the basic profiles,

$$\begin{aligned} \text{KHI: } & U(y) = \tanh(10y), \\ & \bar{\rho}(y) = -\tanh(30y), \quad J = 0.05, \end{aligned} \tag{3.7}$$

$$\begin{aligned} \text{HWI: } & U(y) = 1 + \frac{4}{135}\left(30y - 30 - \log\{\cosh[30(y-1/8)]/\cosh(105/4)\}\right), \\ & \bar{\rho}(y) = -\tanh[30(y+1/8)], \quad J = 0.2, \end{aligned} \tag{3.8}$$

$$\begin{aligned} \text{TCI: } & U(y) = y, \\ & \bar{\rho}(y) = -\frac{1}{2}\left\{\tanh[30(y-1/4)] + \tanh[30(y+1/4)]\right\}, \quad J = 0.14. \end{aligned} \tag{3.9}$$

These profiles have relatively sharp but smooth interfaces in the background density and vorticity and represent 'typical' examples that lead to KHI, HWI, and TCI (respectively). Figure 1 also displays the base profiles and the vorticity and density disturbances associated with their modal eigenfunctions. For the KHI case, $\mathcal{M}_B$ is negligible and there are cancelling contributions through $\mathcal{M}_V$ from the two vorticity interfaces. For HWI, there are equal and opposite contributions to $M = 0$ from $\mathcal{M}_V$ and $\mathcal{M}_B$ that are centered at the vorticity and density interfaces, respectively. For TCI, $\mathcal{M}_V \equiv 0$ and the contributions of each density interface cancel.

3.2. *Pseudomomentum-based mode characterisation*

For arbitrary spatial profiles of vorticity and density, one can exploit the decomposition into $\mathcal{M}_V$ and $\mathcal{M}_B$ to classify instabilities: first, the relative sizes of $|\mathcal{M}_B|$ and $|\mathcal{M}_V|$ indicate whether an interfacial region acts like a density or vorticity interface. Given this "flavour" of the interface, one can then pick out the two largest canceling contributions to M, and thereby classify the instability.

To illustrate this scheme, we solve the linear stability problem analytically for two piece-wise linear profiles. In the first of these examples, a transition occurs from KHI to TCI (Taylor 1931) as the flow parameters are varied, and the distinction between the two becomes ambiguous. Similarly, the second example exhibits a transition between KHI and HWI (Holmboe 1962), and is the flow adopted by Carpenter *et al.* (2010) in applying their diagnostic for distinguishing between these two instabilities.

The first example is Taylor's three-layer flow profile,

$$U(y)=\begin{cases}-1, & \text{if } y\leqslant -1\\ y, & \text{if } -1<y<1\\ 1, & \text{if } y\geqslant 1\end{cases}\qquad\text{and}\qquad \bar{\rho}(y)=\begin{cases}1, & \text{if } y\leqslant -1\\ 0, & \text{if } -1<y\leqslant 1\\ -1, & \text{if } y>1\end{cases}, \tag{3.10}$$

in which there are two, coincident vorticity and density interfaces. The dispersion relation for normal modes is

$$\begin{aligned}&c^4+c^2\left[\frac{e^{-4k}-(2k-1)^2}{4k^2}-1-\frac{J}{k}\right]\\ &\quad+\frac{J^2}{4k^2}\left(1-e^{-4k}\right)-\frac{J}{k}\left(\frac{2k-1+e^{-4k}}{2k}\right)-\left(\frac{e^{-4k}-(2k-1)^2}{4k^2}\right)=0.\end{aligned} \tag{3.11}$$

The pseudomomentum reduces to

$$M=L_x\left[|\hat{\psi}(1)|^2\left(\frac{1}{|1-c|^2}-\frac{2J}{|1-c|^4}\right)+|\hat{\psi}(-1)|^2\left(-\frac{1}{|1+c|^2}+\frac{2J}{|1+c|^4}\right)\right] \tag{3.12}$$

$$\equiv L_x\left[|\hat{\psi}(1)|^2\left(M_V^+-M_B^+\right)+|\hat{\psi}(-1)|^2\left(-M_V^-+M_B^-\right)\right], \tag{3.13}$$

where $M_V^\pm, M_B^\pm>0$ are the magnitudes of the contributions from the upper and lower vorticity and density interfaces, respectively. The unstable normal modes have $|\hat{\psi}(1)|^2=|\hat{\psi}(-1)|^2$, and $c_r=0$ so that $M_V^+=M_V^-$ and $M_B^+=M_B^-$, allowing us to define the relative contribution of the vorticity interfaces as

$$R_1=\frac{M_V}{M_V+M_B}=\frac{1+c_i^2}{1+c_i^2+2J}. \tag{3.14}$$

Then, $R_1=1$ corresponds to pure KHI in the sense that only the vorticity interfaces contribute to the dynamics. Likewise, $R_1=0$ corresponds to pure TCI dynamics, given that only the density interfaces then contribute. Intermediate values of R indicate that all four interfaces play a role in the dynamics. Figure 2(a) shows contours of constant growth rate kc_i on the $k-J$ plane, superposed on a density plot of R_1. For $J=0$, the density variations play no role, implying pure KHI dynamics, and we see that $R_1\to 1$. For $J\gg 1$, $R_1\to 0$, indicating an approach to pure TCI. Between these two limits there is a smooth transition in which all four interfaces play varying roles in the dynamics; the contour $R_1=\frac{1}{2}$, which occurs when $J\approx 0.6$, suggests a convenient distinction between KHI and TCI. However, we emphasize that this distinction is a relative one, and does not imply that only the density interfaces are active when $R_1<\frac{1}{2}$, or that the instability is a pure vorticity interface interaction when $R_1>\frac{1}{2}$.

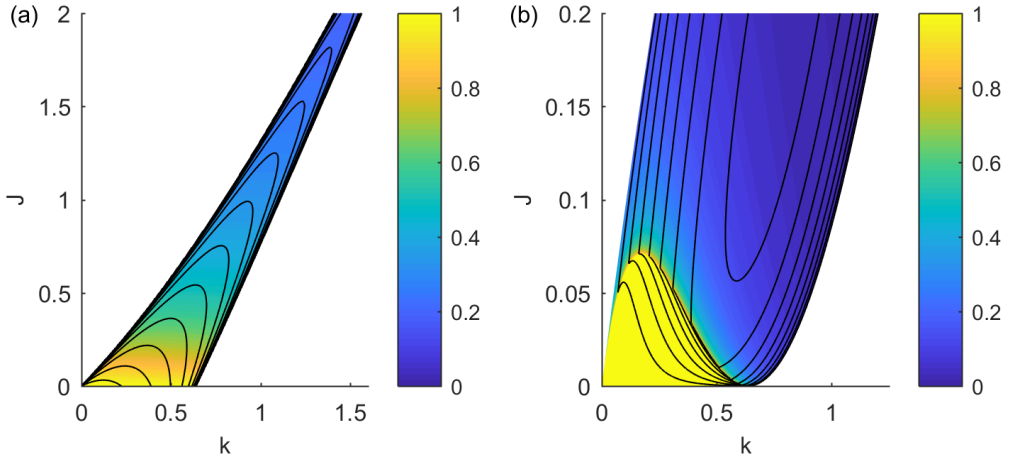

FIGURE 2. (a): Contours of constant growth rate of the unstable mode (black lines) for the linear profile in (3.10) showing the transition between KHI and TCI. The color shading shows a density plot of $R_1 = M_V/(M_V + M_B)$. (b): Contours of constant growth rate of the rightward propagative mode (black lines) for the piecewise linear profile in (3.15) showing the transition between KHI and HWI. The color shading shows a density plot of $R_2 = 1 - |M_B/M_V^+|$, where M_V^+ is the contribution to M_V due to the upper vorticity interface alone.

The second example is Holmboe's flow profile,

$$U(y) = \begin{cases} -1, & \text{if } y \leqslant -1 \\ y, & \text{if } -1 < y < 1 \\ 1, & \text{if } y \geqslant 1 \end{cases} \qquad \text{and} \qquad \bar{\rho}(y) = \begin{cases} 1, & \text{if } y \leqslant 0 \\ 0, & \text{if } y > 0 \end{cases}, \tag{3.15}$$

with dispersion relation,

$$c^4 + c^2\left[\frac{e^{-4k} - (2k-1)^2}{4k^2} - \frac{J}{k}\right] + \frac{J}{k}\left[\frac{e^{-2k} + (2k-1)}{2k}\right]^2 = 0. \tag{3.16}$$

The pseudomomentum is given by

$$M = L_x\left[\frac{|\hat{\psi}(-1)|^2}{2|1+c|^2} - \frac{|\hat{\psi}(1)|^2}{2|1-c|^2} + \frac{2Jc_r|\psi(0)|^2}{|c|^4}\right] \equiv M_V^- + M_V^+ + M_B. \tag{3.17}$$

Figure 2(b) shows contours of constant growth rate kc_i on the k–J plane for the rightward propgating unstable mode. These contours are superposed on a density plot of $R_2 = 1 - |M_B/M_V^+|$. For large wavenuber k, the modal eigenfunctions decay exponentially away from the interfaces, leading to mode interactions that are characterized by cancelling pseudomomentum contributions from just two of $M_V^\pm$ and M_B. For the rightward propagating modes, $R_2 \to 0$ indicates that the instability is generated by the interaction of the upper vorticity interface with the density interface, and has the character of HWI. In view of the symmetry of the profiles, simultaneously there is a leftward traveling HWI with $1 - |M_B/M_V^-| \to 0$. On the other hand, when $R_2 \to 1$, the density interface cannot contribute to the interaction and so the mode must take a KHI character. Indeed, for these flow profiles any mode with zero phase speed $c_r = 0$ has this feature, since M_B then vanishes identically. Intermediate values of R_2 indicate balancing contributions to $M = 0$ from all three of $M_V^\pm$ and M_B. The contour $R_2 = \frac{1}{2}$ again suggests a convenient distinction between KHI-like and HWI-like interactions. As shown in figure 2b, the R_2 diagnostic cleanly

Group	J	k	Re	Pr	Pe	Comments
1	0.14	0.8	300 000	0.6	180 000	
	0.14	0.8	180 000	1	180 000	
	0.14	0.8	60 000	3	180 000	
	0.14	0.8	20 000	10	200 000	
2	0.14	4/3	300 000	0.6	180 000	
	0.14	4/3	180 000	1	180 000	
	0.14	4/3	60 000	3	180 000	
	0.14	4/3	20 000	10	200 000	
3	0.23	4/3	300 000	0.6	180 000	
	0.23	4/3	180 000	1	180 000	
	0.23	4/3	60 000	3	180 000	
	0.23	4/3	20 000	10	200 000	
4	0.3	4/3	300 000	0.6	180 000	
	0.3	4/3	180 000	1	180 000	
	0.3	4/3	60 000	3	180 000	
	0.3	4/3	20 000	10	200 000	
5	0.3	2	300 000	0.6	180 000	
	0.3	2	180 000	1	180 000	
	0.3	2	60 000	3	180 000	
	0.3	2	20 000	10	200 000	
6	0.5	4	300 000	0.6	180 000	
	0.5	4	180 000	1	180 000	
	0.5	4	60 000	3	180 000	
	0.5	4	20 000	10	200 000	
X	0.14	0.8	600	300	180 000	TCI, low Re
	0.5	4	600	300	180 000	TCI, low Re
	0.05	2	25 000	7	175 000	KHI
	0.2	4	180 000	1	180 000	HWI

TABLE 1. Parameter values of simulations. Group X includes additional TCI simulations at low Re and representative KHI and HWI simulations.

identifies the one-sided rightward traveling HWI at higher wavenumber and bulk Richardson number. Moreover, there is an area with $\frac{1}{2} < R_2 < 1$ just above the transition from stationary to propagating waves (highlighted by the sharp changes in the growth-rate contours). Here, the lower vorticity interface plays a role in the mode dynamics, and these propagating instabilities inherit KHI-like character. This result complements the findings of Carpenter *et al.* (2010), but the extent of the region that they identify as KHI is slightly different.

4. TCI simulations

4.1. *Numerical methods and initial conditions*

To simulate TCI, we consider initial-value problems in which small perturbations are added to the base profiles,

$$U(y) = y, \quad \bar{\rho}(y) = -\frac{1}{2}\left\{\tanh[30(y-1/4)] + \tanh[30(y+1/4)]\right\}. \tag{4.1}$$

The perturbations take the form of the unstable mode of the diffusive linear problem associated with these profiles, with an amplitude corresponding to a perturbation energy of $E(0) \approx 10^{-7}$. We solve (2.1)-(2.3) in the domain $y \in [-1, 1]$ and $x \in [0, L_x = 2\pi/k]$, with the horizontal wavenumber k as a parameter.

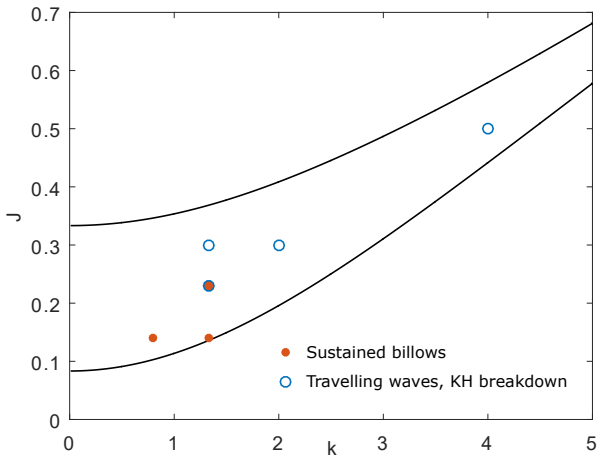

FIGURE 3. Stability boundaries in the (k, J) plane for TCI with background profiles and boundary conditions given by an infinitely sharp interface version of (4.1), along with values of (k, J) for the six groups of simulations listed in table 1. Colours indicate the observed primary dynamics of the saturated instability.

Table 1 lists the parameter values of the simulations conducted. We consider four different pairings of the Reynolds and Prandtl numbers, $(Re, Pr) = (300\,000, 0.6)$, (180 000,1), (60 000,3) and (20 000,10), chosen so that the Péclet number is nearly the same ($Pe = 180,000$ for the first three pairings and 200 000 for the last). The simulations form six groups in the table, so that each group has the same bulk Richardson number J and horizontal wavenumber k, and consists of a simulation from each of the four Reynolds/Prandtl pairings. In addition, group "X" represents an additional set of two TCI simulations at small Reynolds number (though still high Peclet number) at the two extremes of wavelength, plus a pair of representative KHI and HWI computations at comparable Péclet numbers. For the KHI and HWI cases, the initial base states are given by (3.7) and (3.8), respectively.

The locations of the simulations on the $(k, J)-$plane are shown in figure 3. The comparison of the small wavenumber, small bulk Richardson number simulations of group 1 with the high wavenumber, high bulk Richardson number of groups 5 and 6 offers insight into how the mechanism of saturation varies across the strip of instability, which is also drawn in figure 3 (taking the interfaces to be sharp and modes to be inviscid). Groups 2-4, which share the wavenumber $k = 4/3$ but have bulk Richardson numbers that span those of group 1 and group 5, allow one to disentangle any combined effect of varying k and J. Note that the values of k were chosen so that simulations could be compared at different pairings of J and k, whilst trying to ensure that there was at most one unstable mode in the domain to avoid any complication due to mode interactions. The choices do not correspond to the fastest growing mode over all wavenumber at each fixed J, which is a common strategy for constraining parameters in numerical studies. However, the nonlinear dynamics we find for each J appears to be insensitive to the precise choice for k, at least in two dimensions (it is possible that in three dimensions, the secondary instabilities are more sensitive to the choice of k).

The simulations were conducted using Diablo, a parallel Fortran-based numerical integration program developed by Bewley & Taylor (Taylor 2008), which uses a second-order finite difference scheme in the y-direction and a de-aliased Fourier decomposition in x. Time stepping is implemented by a combined implicit-explicit third-order Runge-Kutta-Wray Crank-Nicholson scheme.

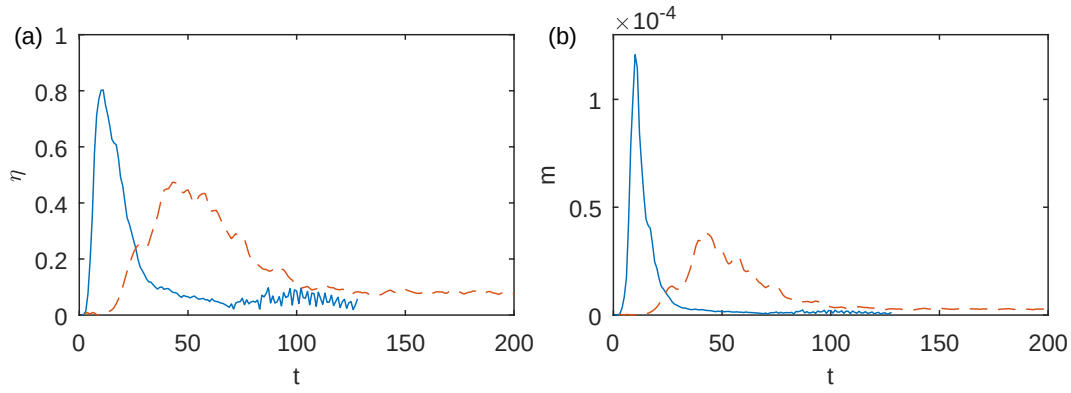

FIGURE 4. (a): Instantaneous mixing efficiency $\eta(t)$ and (b): instantaneous mixing rate $m(t)$ for representative KHI (blue solid) and HWI (red dashed, for which we plot $10m(t)$) simulations.

The grid resolution for the geometry of groups 1–4 is 2048×2048 and for groups 5 and 6 is 1024×2048. Movies illustrating the simulations are provided as Supplementary Information.

4.2. *Diagnostics*

To compare the simulations with one another, we make use of a number of global measures: first, the average perturbation energy $E(t)$ (potential plus kinetic) is defined as

$$E(t) = \frac{k}{8\pi}\int_0^{2\pi/k}\int_{-1}^{1}\left\{[u-U(y)]^2 + v^2 + J[\rho-\bar{\rho}(y)]^2\right\}\,\mathrm{d}y\mathrm{d}x \tag{4.2}$$

(an expansion to second order in mode amplitude connects this quantity to the pseudo-energy $\mathcal{E}$ defined in §3.1; Bühler (2014)). Second, following Peltier & Caulfield (2003), a monotonic adiabatic rearrangement of the current density field $\rho(x,y,t)$ furnishes the background stratification $\rho_*(y,t)$, from which we obtain the background potential energy $P_B(t)$,

$$P_B(t) = -\frac{1}{2}\int_{-1}^{1} Jy\rho_*\,\mathrm{d}y. \tag{4.3}$$

The instantaneous mixing rate $m(t)$ can then found from the time rate of change of $P_B(t)$, correcting for the natural diffusive increase of P_B due to the Péclet number:

$$m(t) = \frac{\mathrm{d}P_B}{\mathrm{d}t} - \frac{J}{Pe}. \tag{4.4}$$

Third, the mixing efficiency $\eta(t)$ is given by

$$\eta(t) = \frac{m(t)}{m(t)+D(t)}, \tag{4.5}$$

where the dissipation rate is

$$D(t) = \frac{k}{4\pi Re}\int_0^{2\pi/k}\int_{-1}^{1}\left[\left(\frac{\partial u}{\partial x}\right)^2 + \left(\frac{\partial u}{\partial y}\right)^2 + \left(\frac{\partial v}{\partial x}\right)^2 + \left(\frac{\partial v}{\partial y}\right)^2\right]\,\mathrm{d}y\mathrm{d}x. \tag{4.6}$$

It should be emphasised that for the two-dimensional simulations presented here, the mixing efficiencies are expected to be significantly higher than typical values for three-dimensional flow; two-dimensional flows dissipate far less than their three-dimensional counterparts (e.g. Peltier & Caulfield 2003). Nevertheless, we find the mixing efficiency to be a useful indicator to distinguish

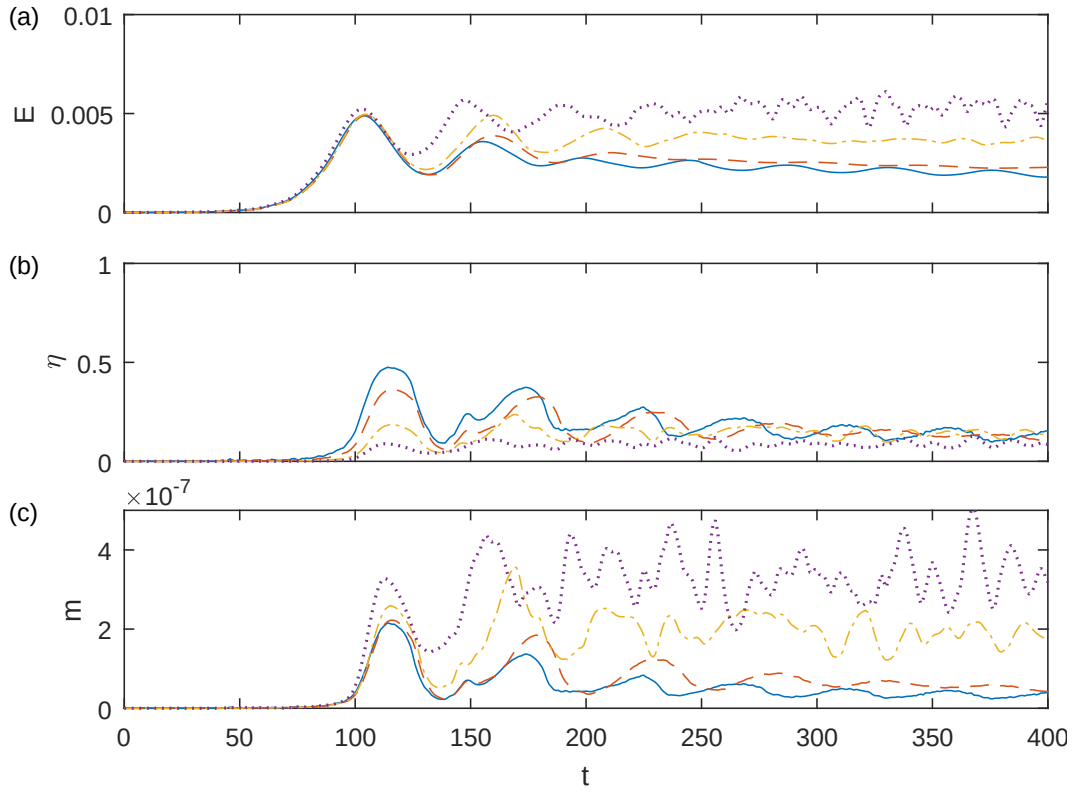

FIGURE 5. Time evolution of (a): the perturbation energy $E(t)$, (b): mixing efficiency $\eta(t)$ and (c): mixing rate $m(t)$ for the simulations in group 1, with $(Re, Pr) = (300\,000, 0.6)$ (blue solid), (180 000,1) (red dashed), (60 000,3) (yellow dot-dashed), and (20 000,10) (purple dotted).

between our simulations in addition to the perturbation energy density $E(t)$ since it is possible to have energetic flows which do little mixing and vice versa. The final scene is set for our discussion of the mixing character of TCI by figure 4, which shows $\eta(t)$ and $m(t)$ for the representative KHI and HWI computations of table 1, and illustrates the vigorous, but short-lived mixing of KHI and the lower, but more long-lived action of HWI.

4.3. *Small k, small J dynamics (group 1)*

4.3.1. *Energetic characteristics*

Figure 5 shows the time evolution of $E(t)$, $\eta(t)$ and $m(t)$ for group 1, for each of the four (Re, Pr) pairings. The initial evolution of the perturbation energy $E(t)$ collapses onto the same curve during the initial linear growth and peaks around $t = 100$ for all four simulations. Subsequently, $E(t)$ settles into a decaying oscillation for the $(Re, Pr) = (300\,000, 0.6)$ and (180 000,1) simulations; the (60 000,3) simulation levels off somewhat, whereas the (20 000,10) simulation transitions to a much higher amplitude, chaotic state.

During the linear growth, the mixing efficiency $\eta(t)$ and rate $m(t)$ remain small, but increase substantially after the first maxima in $E(t)$. The four simulations reach different peak efficiencies, mainly because of the enhanced dissipation at lower Re; the time evolution of the mixing rate $m(t)$ through the first peak is more comparable between the simulations. Evidently, the simulations with higher Prandtl numbers ($Pr = 3$ and 10) experience higher levels of sustained mixing than in the lower Prandtl number cases ($Pr = 0.6$ and 1).

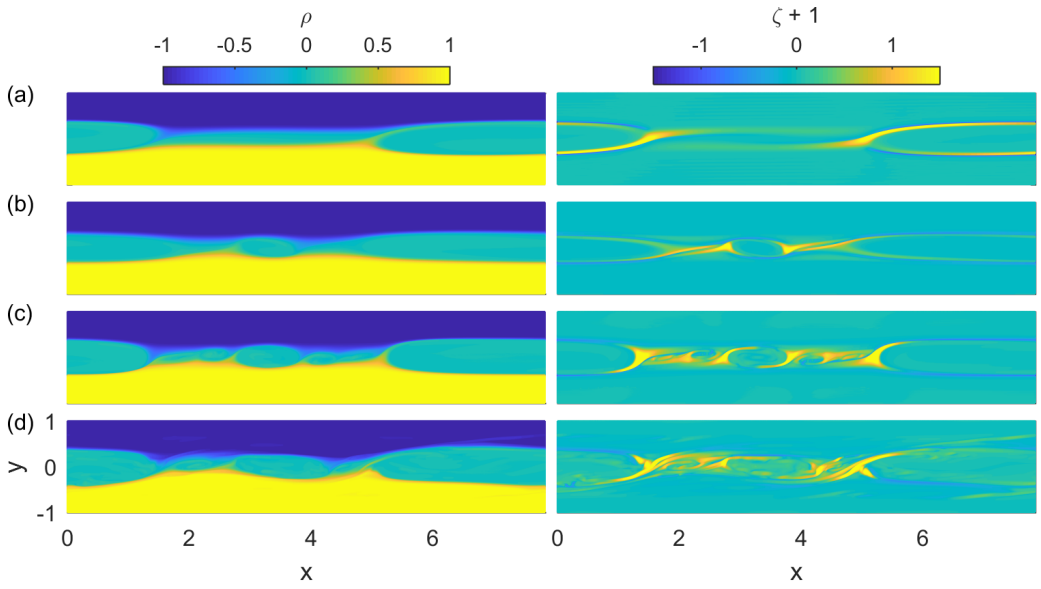

FIGURE 6. Snapshots of the density $\rho(x, y, t)$ (left) and vorticity $\zeta(x, y, t)+1$ (right) for four different times and parameter values in group 1. (a): $(Re, Pr) = (300\,000, 0.6)$ at $t = 110$, (b): $(Re, Pr) = (180\,000, 1)$ at $t = 141$, (c): $(Re, Pr) = (20\,000, 10)$ at $t = 188$ and (d): $(Re, Pr) = (20\,000, 10)$ at $t = 375$. Colorbars show density (left) and vorticity (right).

4.3.2. *Billow structure*

Figure 6 collects snapshots of the density $\rho(x, y, t)$ and vorticity $\zeta(x, y, t)$ at a number of key times in simulations of group 1. Figure 6(a) shows the $(Re, Pr) = (300\,000, 0.6)$ simulation. During the initial linear evolution of this TCI, sinusoidal deformations develop that locally bring the density interfaces together. Instead of meeting and pinching off, however, the perturbations develop into cuspy structures that become swept sideways by the mean flow to create a distinctive billow with a large horizontal extent and associated filaments of baroclinic vorticity. This initial evolution is shared by all four simulations in group 1, and the billow corresponds to the primary nonlinear structure observed previously by Lee & Caulfield (2001) and Balmforth *et al.* (2012).

At slightly later times, as illustrated by the $(Re, Pr) = (180\,000, 1)$ simulation shown in figure 6(b), a 'secondary' billow appears in the gap between the cusps of the primary billow. Again, this feature appears in all the simulations of group 1 and was observed by Lee & Caulfield (2001). More interestingly, with higher Prandtl number, further billows appear at yet later times, in the manner of a cascade to smaller scales. Figure 6(c) shows the $(Re, Pr) = (20\,000, 10)$ simulation at $t = 188$ in which 'tertiary', and possibly even 'quarternary' billows of decreasing size have formed after the secondary billow. This cascade of billows is robust to variations in Reynolds and Prandtl number, occuring also in the low-Re TCI simulation with $(J, k, Re, Pr) = (0.14, 0.8, 600, 300)$.

4.3.3. *Billow cascade as a secondary TCI*

Figure 7 shows the gradient Richardson number $-J\rho_y/u_y^2$ for vertical profiles of ρ and u, horizontally averaged over a region $2.4 < x < 4.2$ outside the primary billow in the top row of images of figure 6. Also shown is the corresponding initial condition. The region outside the primary billow retains two relatively strong density interfaces, but their vertical separation has changed, which suggests that the region may still be susceptible to TCI. Indeed, one can use the horizontal averages of ρ and u over this region, together with an adjusted wavenumber of $k = 3$ consistent

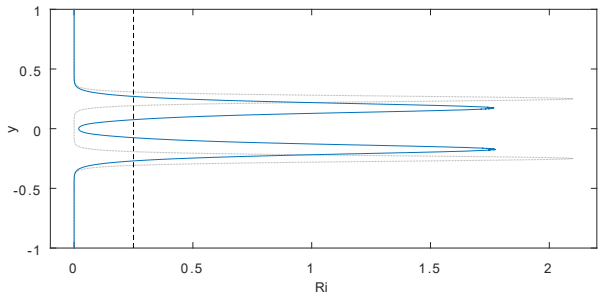

FIGURE 7. Gradient Richardson number $-J\rho_y/u_y^2$ for the horizontally averaged buoyancy and velocity profiles in the region between the billow $2.4 < x < 4.2$ for the $(Re, Pr) = (300\,000, 0.6)$ group 1 simulation at $t = 110$ (blue), along with the gradient Richardson number for the initial condition (grey, dotted) Also shown is the value $Ri = 0.25$ (black dashed).

with its rough horizontal extent, to conduct a second linear stability analysis. This calculation reveals a TCI with a growth rate of about 0.1. By contrast, the initial basic state is not unstable at $k = 3$. Thus, the nonlinear distortion of the mean profile by the primary instability generates a secondary TCI, and occurs because the original instability moves the density interfaces closer together to reduce the local length-scale. Moreover, the density interfaces remain sharp through the combined action of the relatively high Péclet number limiting the diffusive effects and a favourable straining flow induced by the primary billow. Evidently, this mechanism continues to operate at higher Prandtl numbers, yielding further secondary instabilities and generating the cascade described above.

4.3.4. *Final attrition and secondary nonlinear Holmboe waves*

For the lower Prandtl number simulations, the primary billows slowly pulsate and diffusively decay, generating the decaying oscillations in $E(t)$. Eventually, the secondary billows drift sideways to become consumed by the larger primary billow. In the $Pr = 10$ simulations, however, a large amplitude, long wavelength, parasitic nonlinear Holmboe wave develops on top of the array of billows, much as in the earlier computations of Balmforth *et al.* (2012) and Eaves & Caulfield (2017). This is illustrated in figure 6(d); the parasitic Holmboe wave is evidenced by the filaments of baroclinic vorticity drawn out from the main billow towards the right-hand side of the domain. This prolonged Holmboe wave activity accounts for the sustained levels of perturbation energy $E(t)$, mixing efficiency $\eta(t)$ and mixing rate $m(t)$ in this simulation. Note that the base flow $U(y) = y$ does not contain any inflection points; as detailed by Eaves & Caulfield (2017), the emergence of nonlinear Holmboe waves results after the nonlinear rearrangement of the mean velocity field due to the saturation of the primary TCI and its introduction of flow curvature. Evidently, it is only at large Pr that the density interfaces remain sufficiently sharp in comparison to the baroclinically generated vorticity filaments bordering the billows to permit the secondary HWI (the Prandtl number dictates the relative diffusion of density and vorticity).

4.4. *Large k, large J dynamics (groups 5–6)*

4.4.1. *Energetic characteristics*

Figure 8 shows the time evolution of $E(t)$, $\eta(t)$ and $m(t)$ for the $(k, J) = (2, 0.3)$ simulations of group 5 and the $(k, J) = (4, 0.5)$ simulations of group 6. Once more, the simulations show the same initial linear growth of the perturbation energy $E(t)$. The peak in $E(t)$ is again followed by decaying oscillations about a slowly diffusing nonlinear state at lower Pr, or sustained higher-frequency oscillations symptomatic of emergent parasitic Holmboe waves at larger Pr. As for the group 1 simulations, the mixing efficiency $\eta(t)$ and rate $m(t)$ increase to significant levels

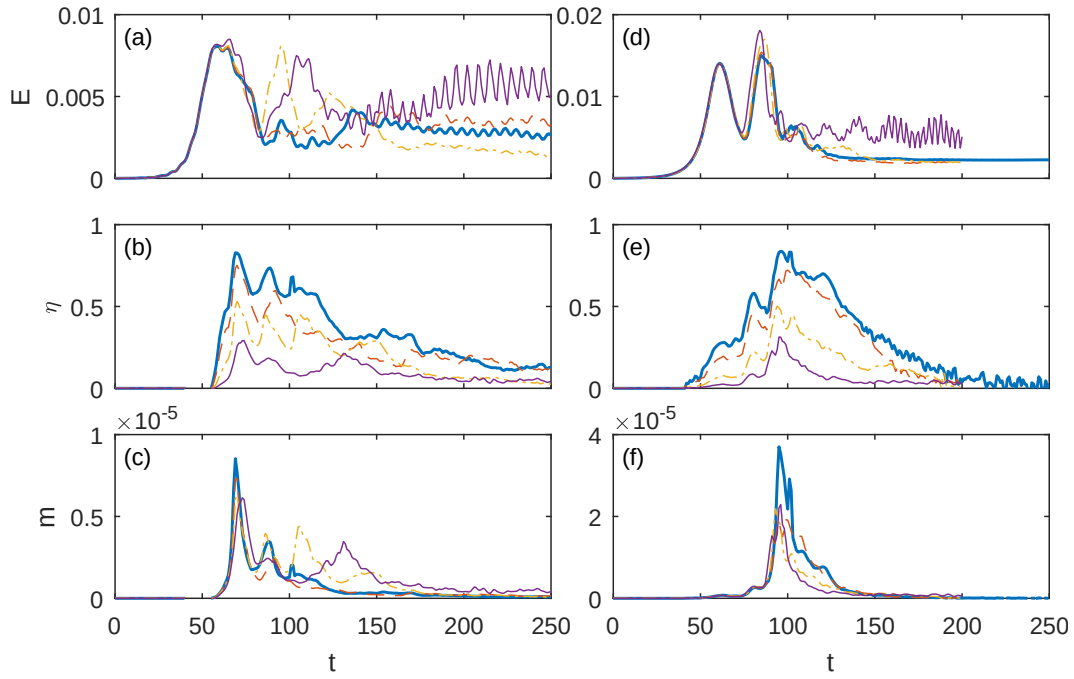

FIGURE 8. Time evolution of (a,d): the perturbation energy $E(t)$, (b,e): mixing efficiency $\eta(t)$ and (c,f): mixing rate $m(t)$ for the simulations in (a-c): group 5 and (d-f): group 6, with $(Re, Pr) = (300\,000, 0.6)$ (blue thick solid), (180 000,1) (red dashed), (60 000,3) (yellow dot-dashed), and (20 000,10) (purple thin solid).

only after the end of the phase of linear growth. The maximum values reached, however, are substantially higher and are comparable to those observed for two-dimensional KHI simulations (see Peltier & Caulfield 2003, and figure 4). The implied enhanced mixing events have only previously been associated with KHI; we uncover the origin of this presently.

4.4.2. *Billow break-up*

Figure 9 shows snapshots of the density $\rho(x, y, t)$ and vorticity $\zeta(x, y, t)$ at a number of key times in the simulations of group 5. Figures 9(a,b) show the $(Re, Pr) = (60\,000, 3)$ simulation; once again, during the linear growth of the TCI, cusp-like deformations appear on each density interface and are swept sideways by the mean flow. This time, however, the resulting nonlinear traveling waves do not collide and merge to form a billow. Instead, they retain their identity and generate more baroclinic vorticity due to the higher bulk Richardson number; these alternative primary nonlinear structures correspond to the cuspy wave observed by Eaves & Caulfield (2017). Moreover, the waves interact strongly to draw out large-amplitude filaments of vorticity as time progresses. These filaments subsequently roll up through localised KHI-type secondary instabilities, creating vortices throughout the middle density layer and precipitating a vigorous mixing event, as illustrated by figures 9(c,d) from the $(Re, Pr) = (60\,000, 3)$ simulation. Eventually, the finer-scale vortices viscously decay, coarse-graining a residual nonlinear structure (see figure 9(f)). At long times, a parasitic Holmboe wave emerges for $Pr = 10$ (see figure 9(e)).

Figure 10 collects snapshots of $\rho(x, y, t)$ and $\zeta(x, y, t)$ from simulations of group 6. The horizontal extent of the domain is now sufficiently short that the cuspy nonlinear traveling waves no longer lock into place when they approach, but pass by one another to create complex vorticity dynamics in the middle density layer; sharp filaments of vorticity once more appear and subse-

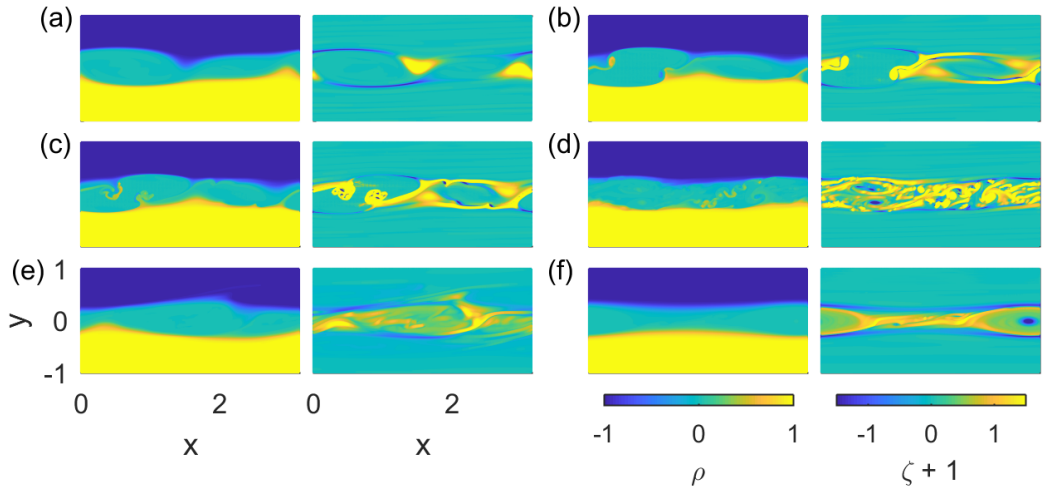

FIGURE 9. Snapshots of the density $\rho(x, y, t)$ (left) and vorticity $\zeta(x, y, t) + 1$ (right) for six different times and parameter values in group 5. (a): $(Re, Pr) = (60\,000, 3)$ at $t = 56$ and (b): at $t = 66$, (c): at $t = 68$ and (d): at $t = 86$. (e): $(Re, Pr) = (20\,000, 10)$ at $t = 240$ and (f): $(Re, Pr) = (300\,000, 0.6)$ at $t = 250$.

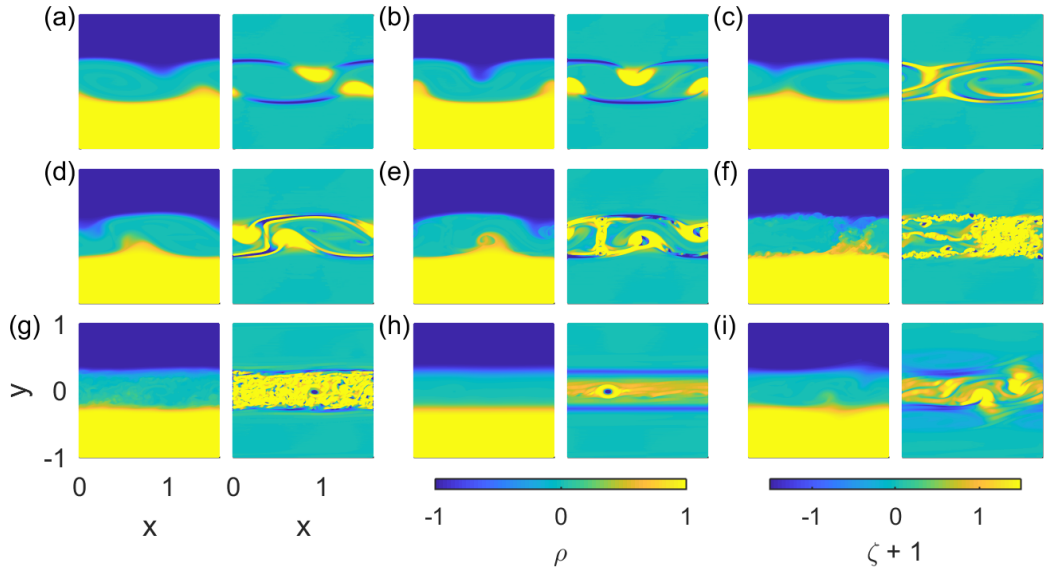

FIGURE 10. Snapshots of the density $\rho(x, y, t)$ (left) and vorticity $\zeta(x, y, t) + 1$ (right) for nine different times and parameter values in group 6. $(Re, Pr) = (300\,000, 0.6)$ at (a): $t = 55$, (b): $t = 62$ and (c): $t = 74$, (d): $t = 82$, (e): $t = 88$ and (f): $t = 95$, (g): $t = 124$ and (h): $t = 250$ and (i): $(Re, Pr) = (20\,000, 10)$ at $t = 200$.

quently roll up due to secondary KHI (see figures 10(d-f)). This fills the central density layer with finer scale vortical structures that again viscously decay to a smoother state but for the emergence of parasitic Holmboe waves at $Pr = 10$, as seen in figures 10(g-i).

The roll-up of baroclinically generated vorticity filaments *via* secondary KHI rationalizes the heightened mixing efficiencies and rates in the simulations of groups 5 and 6; the primary TCI itself generates very little mixing. Because the secondary roll-ups span the entire middle density

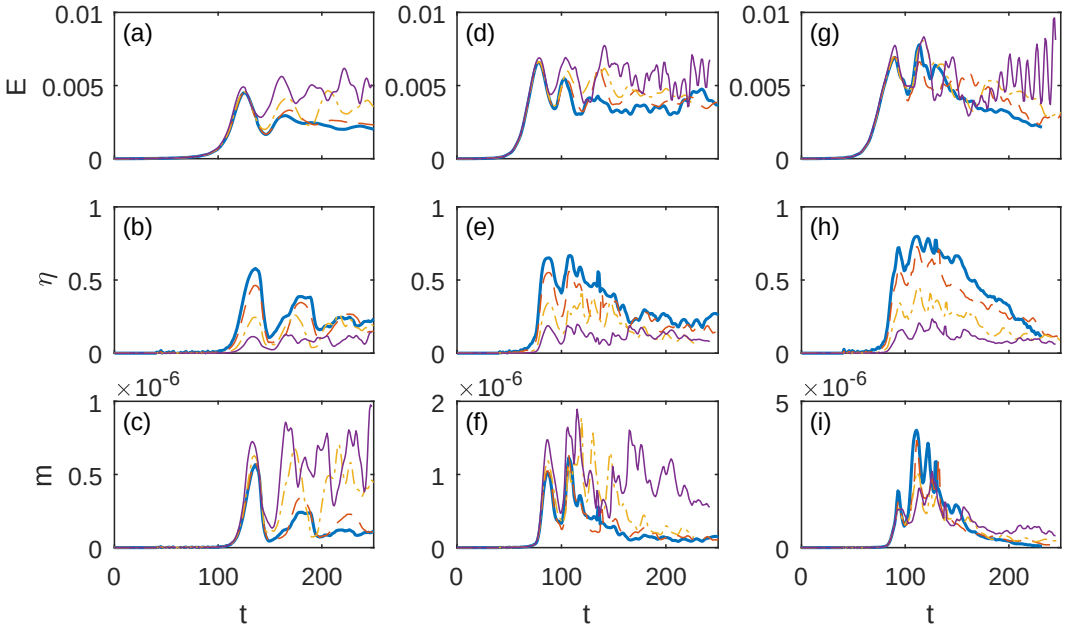

FIGURE 11. Time evolution of (a,d,g): the perturbation energy $E(t)$, (b,e,h): mixing efficiency $\eta(t)$ and (c,f,i): mixing rate $m(t)$ for the simulations in (a-c): group 2, (d-f): group 3 and (g-i): group 4, with $(Re, Pr) = (300\,000, 0.6)$ (blue thick solid), (180 000,1) (red dashed), (60 000,3) (yellow dot-dashed), and (20 000,10) (purple thin solid).

layer, the mixing efficiency reaches values more typically associated with a primary KHI. The baroclinic generation of vorticity arises through the term $J\rho_x$ in (2.3), and so can be associated with either large values of J or with small horizontal length scales. The simulations of groups 5 and 6 possess both attributes in comparison to group 1, and so it remains unclear whether the secondary behaviour is due to a larger J or smaller horizontal wavenumber k. The simulations of groups 2, 3 and 4, described below, indicate that the bulk Richardson number J is chiefly responsible.

Unlike the cascade of Taylor–Caulfield billows for weaker stratification in larger domains, the destruction of saturated TCI states by secondary KHI roll up is *not* robust to changes in Reynolds number. This is indicated by the $(J, k, Re, Pr) = (0.5, 4, 600, 300)$ TCI simulation which shows the emergence of large amplitude, cuspy nonlinear traveling waves on each density interface. These waves interact relatively weakly, however, and propagate past each other without forming any small scale vorticity filaments due to the higher viscosity. The waves thereby slowly decay without any small-scale KHI roll-up. Such Re-dependent secondary KHI roll-up also distinguishes the two simulations presented by Eaves & Caulfield (2017).

4.5. *Intermediate k, varying J dynamics (groups 2–4); KHI roll-up versus TCI cascade*

Figure 11 shows the time evolution of $E(t)$, $\eta(t)$ and $m(t)$ for groups 2, 3 and 4. The plots of mixing efficiency $\eta(t)$ and rate $m(t)$ illustrate how the small $J = 0.14$ simulations of group 2 resemble those of group 1, whereas the large $J = 0.3$ simulations of group 4 are more similar to group 5. The evolution of $\eta(t)$ and $m(t)$ for the intermediate $J = 0.23$ simulations of group 3 appears to blend the behaviours of groups 2 and 4.

Figure 12 collects snapshots from simulations of groups 2, 3 and 4. Figure 12(a), from the $(Re, Pr) = (20\,000, 10)$ simulation with $J = 0.14$, illustrates how secondary and tertiary billows again appear in addition to the primary billow, much as in the simulations of group 1 but

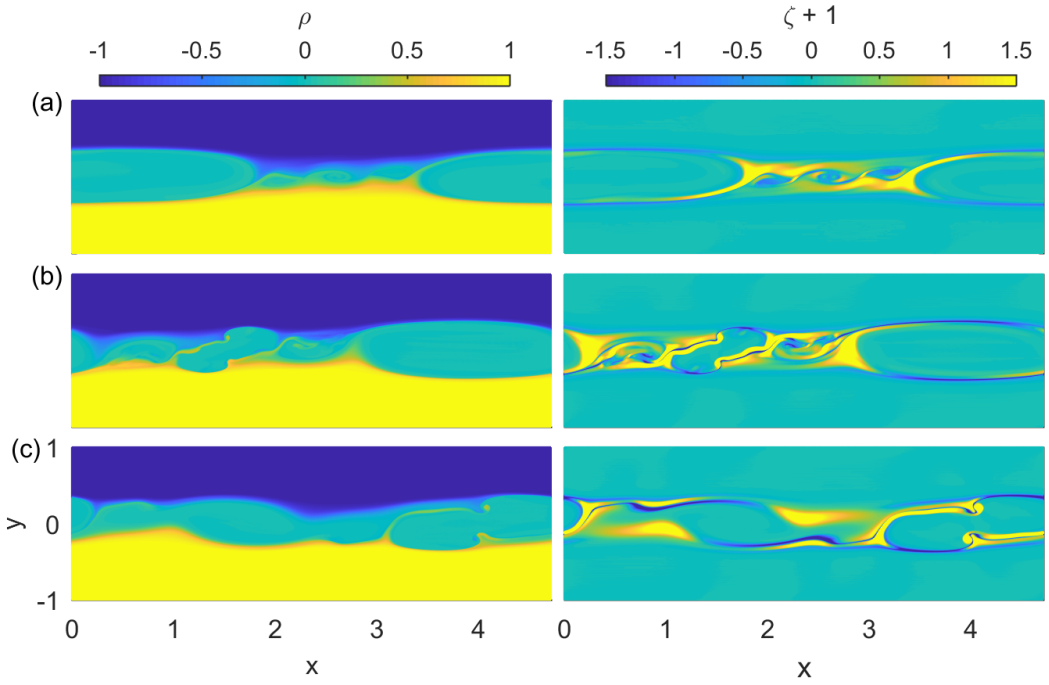

FIGURE 12. Snapshots of the density $\rho(x, y, t)$ (left) and vorticity $\zeta(x, y, t) + 1$ (right) for three different times and parameter values in groups 2, 3 and 4. (a): $(Re, Pr) = (20\,000, 10)$ for $J = 0.14$ at $t = 169$, (b): $J = 0.23$ at $t = 104$, (c): and $J = 0.3$ at $t = 93$.

now over a shorter horizontal domain. In figure 12(b), taken from the $(Re, Pr) = (20\,000, 10)$ simulation with $J = 0.23$, a cascade of billows almost forms, but at the expense of large baroclinic vorticity generation in the region outside the primary billow. Secondary KHIs then occur over that region, but the primary billow is shielded from their destructive effect and persists to the end of the simulation. Finally, figure 12(c) shows the cascade of billows forming in the $(Re, Pr) = (20\,000, 10)$ simulation with $J = 0.3$. This time, the billows all suffer secondary KHI due to the elevated baroclinic vorticity generation; small-scale vortices then fill middle layer, as in the simulations of groups 5 and 6.

4.6. *Nonlinear TCI phenomenology*

To summarise, the nonlinear saturation of TCI creates a cascade of billow-like structures at small J, cuspy traveling waves that draw out tight vorticity filaments and induce vigorous mixing via small-scale KHI at large J, and parasitic nonlinear Holmboe waves at large Pr. The occurance in the (k, J) plane of the former two primary saturation dynamics are shown in figure 3. The two latter features are captured and summarized in figure 13. Figure 13(a) plots the maximum mixing rate, $\max[m(t)]$, for all TCI simulations in groups 1–6 against the corresponding value of J. The maximum mixing rate increases almost exponentially with J, quantifying the mixing associated with the observed breakdown to small-scale KHI. Figure 13(b) plots a measure of the vertical excursions of the two density interfaces, $\overline{h_\rho}$, against Prandtl number. This quantity is computed from the contours along which $\rho(x, y_\pm, t) = \pm\frac{1}{2}$: we first determine the instantaneous excursions, $h_\rho^\pm(t) \equiv \max_x(y_\pm) - \min_x(y_\pm)$, and then average $h_\rho = [h_\rho^+(t) + h_\rho^-(t)]/2$ over late times to obtain $\overline{h_\rho}$. Parasitic Holmboe waves generate localised large amplitude vertical motions,

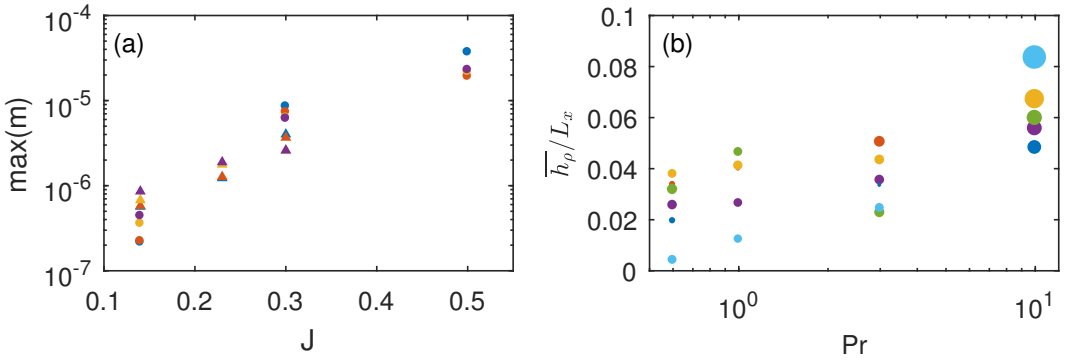

FIGURE 13. (a): Peak mixing rate as a function of J for all simulations. Groups 1 and 5–6 (circles) and groups 2–4 (triangles) for $(Re, Pr) = (300\,000, 0.6)$ (blue), (180 000,1) (red), (60 000,3) (yellow) and (20 000,10) (purple). (b): Late-time, time-averaged vertical excursion $\overline{h_\rho}$ of the $\rho = \pm\frac{1}{2}$ density contours, normalised by $L_x = 2\pi/k$ and plotted against Prandtl number. Groups 1 (dark blue), 2 (red), 3 (yellow), 4 (purple), 5 (green) and 6 (light blue). The size of the points indicates the standard deviation of h_ρ, again normalised by L_x.

and are therefore identified by elevated levels of h_ρ and its standard deviation, as in the $Pr = 10$ simulations.

To address the question of how robust these finding are when we progress from two to three spatial dimensions, we conducted a single simulation in 3D corresponding to the $(Re, Pr) = (20\,000, 10)$ simulation of group 6. Even for the relatively small domain of this simulation, the resolution requirements at $Pe = 200\,000$ are substantial. In order to make the 3D computation manageable, we use the 2D simulation at $t = 50$ as an initial condition with spanwise wavenumber 2π, adding extra low-level noise to force 3D dynamics, and then continue the simulation up to $t = 100$. The added noise changed the perturbation kinetic energy from 4.28×10^{-4} to 5.15×10^{-4}. Figure 14 compares $E(t)$ for the 2D and 3D simulations. The 3D simulation shadows the 2D simulation for much of its evolution, but begins to deviate at $t = 93$. Nevertheless, the 3D simulation follows the 2D simulation for sufficiently long to exhibit the same breakdown to small-scale KHI roll-ups. In figure 15(a) we show surfaces of the two density interfaces $\rho = \pm\frac{1}{2}$ for the 3D simulation at $t = 100$. Three-dimensionality is clearly visible. Figure 15(b-d) also compare a 2D slice through the full 3D density field with the density field of the 2D computation. As highlighted by the detachment of a feature from a density interface, the 2D solution at $t = 102$ shows most similarity with the 3D slice at $t = 100$, indicating a slight lengthening of the timescales in 3D. Thus, at least for the addition of weak 3D noise, it appears that the breakdown to small-scale secondary KHI is a robust phenomenon for TCI at large k and J.

5. Steady nonlinear characterisation

5.1. *Streamfunction relations of the saturated states*

Without dissipation (i.e. $Pe, Re \to \infty$), the equations of motion admit steady nonlinear wave solutions (Long 1953) that satisfy, in the frame of the wave, the relations

$$\zeta = \nabla^2\psi, \qquad \rho = \mathcal{R}(\psi), \qquad \zeta = Jy\frac{\mathrm{d}\mathcal{R}}{\mathrm{d}\psi} + \mathcal{L}(\psi), \tag{5.1}$$

for two arbitrary functions, $\mathcal{R}(\psi)$ and $\mathcal{L}(\psi)$. These streamfunction relations can be used to nonlinearly characterise the states which result after the saturation of KHI, HWI and TCI.

To illustrate the construction, we use simulations in which secondary instabilities do not im-

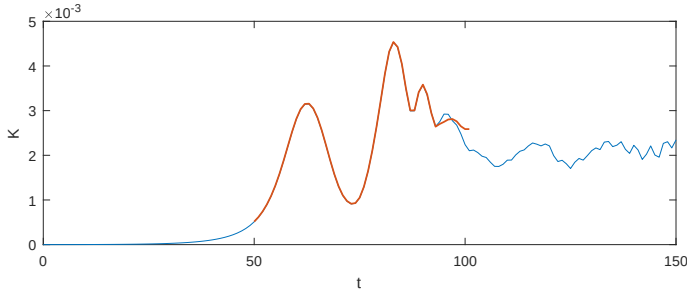

FIGURE 14. Evolution of the perturbation kinetic energy for the 2D simulation with $(\mathrm{Re}, \mathrm{Pr}) = (20\,000, 10)$ in group 6 (thin blue) and a 3D simulation initialised by randomly perturbing the 2D simulation at $t = 50$ (thick red).

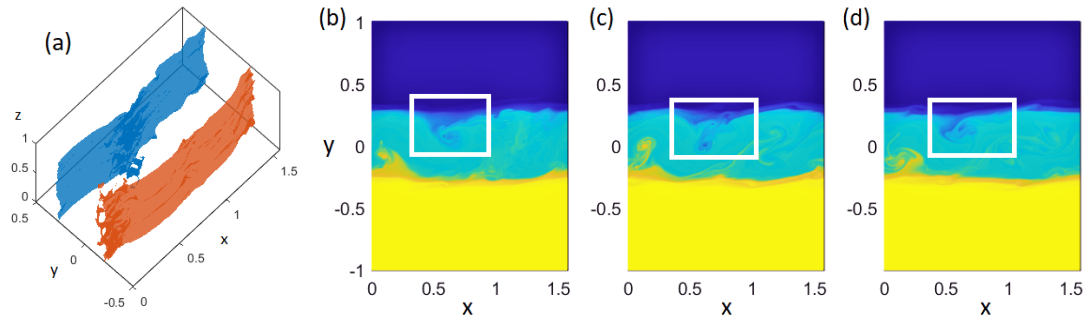

FIGURE 15. (a): Surfaces of $\rho = -\frac{1}{2}$ (blue) and $\rho = \frac{1}{2}$ (red) at $t = 100$ for a $(\mathrm{Re}, \mathrm{Pr}) = (20\,000, 10)$ 3D simulation simulation of group 6. (b): Vertical slice through the 3D density field at $t = 100$, and (c,d): the 2D density fields at $t = 100$ and 102. White boxes highlight a feature detaching from the upper density interface. Density colorbar as in figures 6, 9, 10 and 12.

mediately destroy the nonlinear states reached at saturation, but viscous diffusion smooths the structures to furnish slowly evolving nonlinear waves. Unfortunately, scatter plots of the solution at each point of the computational domain at a representative time provide poor representations of the effective streamfunction relations because of the small residual time-dependence of the solutions and the need to differentiate the density relation. We therefore perform averages of ρ, ζ and y over streamlines within the domain for a flow snapshot towards the end of each simulation, and then use these averages and their derivatives to construct $\mathcal{R}(\psi)$ and $\mathcal{L}(\psi)$. More specifically, from the representative snapshot of the solution, we identify the streamlines from the contours of $\psi(x, y, t) = c$, for a set of constant values c, and then average the density and vorticity fields and y over these curves. The former provides the relation $\rho = \mathcal{R}(c) = \mathcal{R}(\psi)$; this function can be differentiated numerically in c and combined with the averages of y, denoted by $Y(c)$, and of ζ, denoted by $Z(c)$, to arrive at $\mathcal{L}(\psi) = \mathcal{L}(c) = Z(c) - J\,Y(c)\mathcal{R}'(c)$.

The results of this averaging procedure are shown in figures 16–18 for the representative KHI and HWI computations and the TCI simulation with $(Re, Pr) = (180\,000, 1)$ from group 1. The figures display the final density and vorticity fields used for the analysis, and the resulting streanfunction relations. Also included are scatter plots of ρ and $\zeta - Jy\mathcal{R}'(\psi)$ against ψ taken from a subset of the grid-points, using the streamline-averaged $\mathcal{R}(\psi)-$function. The variability of this data about the streamline average curves is mostly indicative of residual time dependence. Note that in the case of HWI, the non-zero phase speed of the final nonlinear state was subtracted

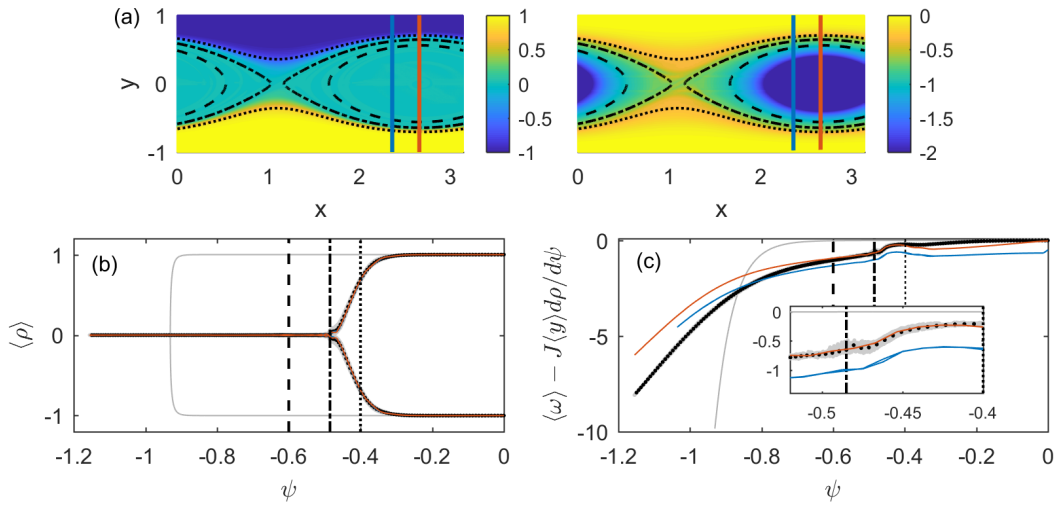

FIGURE 16. (a): Density field (left) and vorticity field (right) of the final state of the representative KHI simulation. Functional relationships (b): $\mathcal{R}$ and (c): $\mathcal{L}$ found from averaging over streamlines shown with black dots. Light grey lines show functional relations of the initial condition. Vertical lines indicate streamfunction values corresponding to the streamlines overlain on the density and vorticity fields. Colored lines show approximations to the functional relationships $\mathcal{R}(\psi)$ and $\mathcal{L}(\psi)$ from individual sparse 1D profiles of density ρ, horizontal velocity u and dissipation ϵ, where the streamfunciton $\psi \approx \int u dy$ and the vorticity $\zeta \approx -\sqrt{\epsilon}$ at $x = 2.36$ (blue) and $x = 2.66$ (red). Red and blue lines in (a) show these x-locations in the spatial density and vorticity fields. Grey dots show relations taken from scattered values of ρ, ψ and ζ at $1/100^{th}$ of the total grid points, where $\mathrm{d}\mathcal{R}/\mathrm{d}\psi$ is taken from the smooth black data.

from the velocity field prior to calculating the streamfunction in order to shift into the wave frame.

The KHI solution in figure 16 displays a clear three-branch structure for $\mathcal{R}$, reflective of the existence of three density layers. The middle density layer with $\rho \approx 0$ is not present in the initial condition but corresponds to the well mixed region forming at the core of the overturning KH billow, and forms the long left-hand tail of the $\rho - \psi$ relation. The plot of $\mathcal{L}$ is reminiscent of Stuart's cat's eye vortex solution for unstratified shear flow (Stuart 1967), for which $\zeta \propto \exp(-2\psi)$. The only significant deviation from such a smooth curve is the slight kink that arises as one moves across the border of the KH billow and the baroclinic term $Jy\mathrm{d}\mathcal{R}/\mathrm{d}\psi$ enters the fray.

The HWI solution in figure 17 again has a three-branch structure for $\mathcal{R}$, even though there are only two distinct density layers. The complication arises because two pieces of the $\mathcal{R}$ function have $\rho \approx -1$, one of which corresponds to the upper density layer whereas the other (left-hand) part characterizes the vortex propagating above the density interface. That vortex draws a filament of dense fluid away from the density interface to generate the familiar cusp-like form of the Holmboe wave; the entrainment of this fluid into the vortex slightly elevates its density above the original level of -1. The plot of $\mathcal{L}$ is also fairly complex, with three distinct branches corresponding to the two density layers and the vortex.

The TCI relations of figure 18 preserve the three-branch structure for $\mathcal{R}$ of the initial condition. Unlike the corresponding KHI relation, the tail of the $\rho - \psi$ relation in the central density layer $\rho = 0$ is very short, indicating a much weaker circulation than for KHI. This feature distinguishes the Taylor–Caulfield billow from the strong vorticity-driven overturning of KHI.

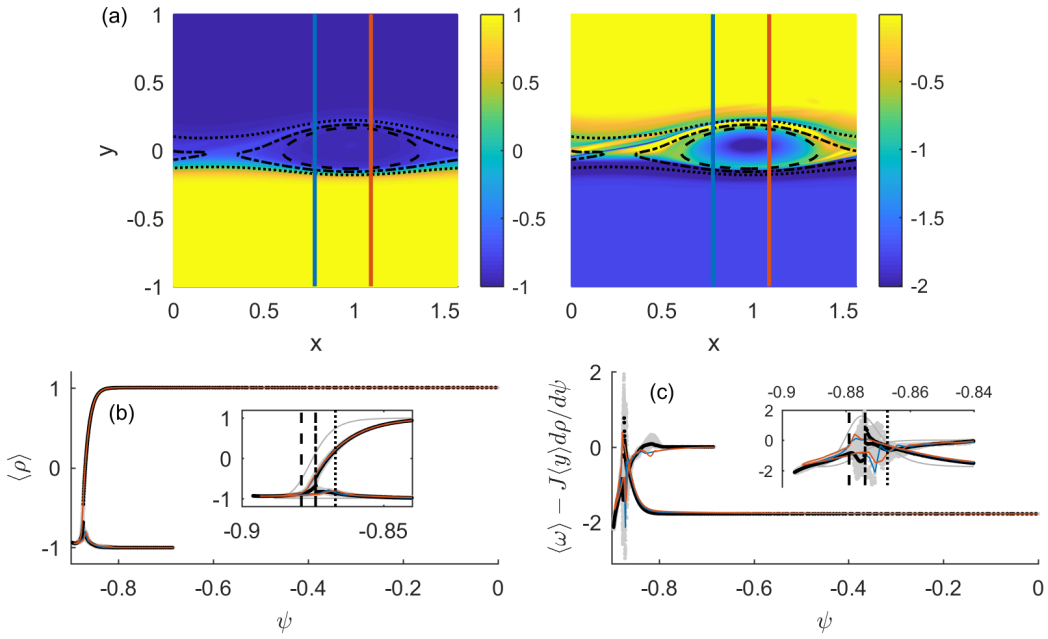

FIGURE 17. A similar plot to figure 16, but for the representative HWI simulation. The approximate relations built from 1D profiles are taken at $x = 0.78$ (blue) and $x = 1.09$ (red).

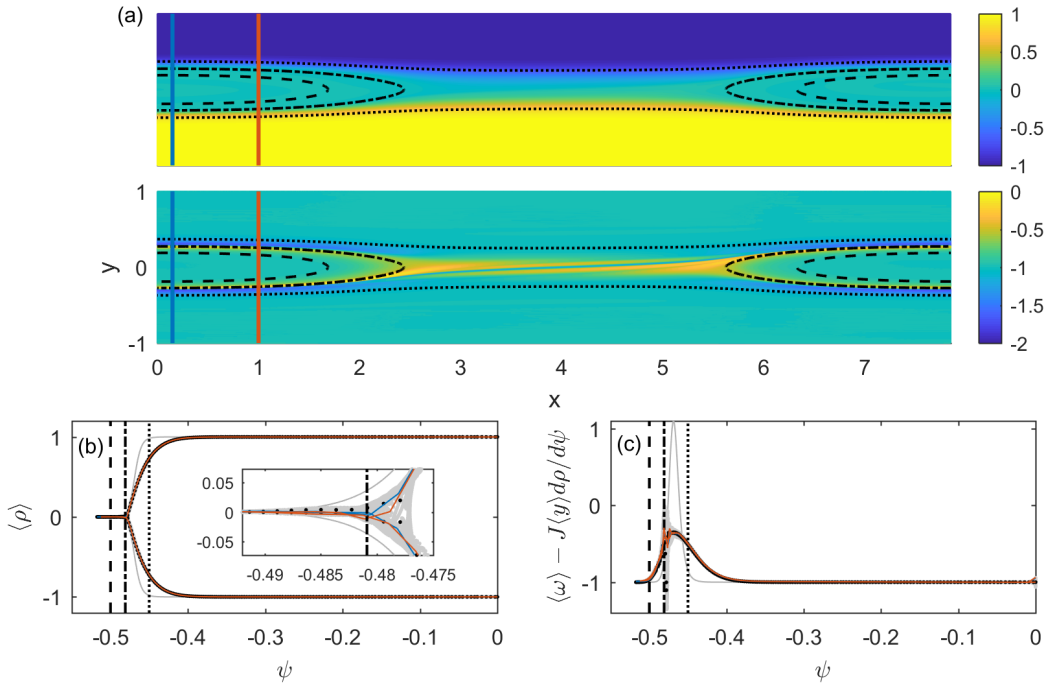

FIGURE 18. A similar plot to figure 16, but for the TCI simulation with $(\mathrm{Re}, \mathrm{Pr}) = (180\,000, 1)$ from group 1. The approximate relations built from 1D profiles are taken at $x = 0.1$ (blue) and $x = 1$ (red).

Further distinction with KHI is made when examining $\mathcal{L}$, which has a rather different, non-monotonic form for TCI inherited from the initial condition.

The streamfunction relations can also be built approximately using vertical profiles cutting through the nonlinear structures, such as might be furnished by observational measurements. Such observations do not readily access the streamfunction or vorticity. Instead, to mirror a reconstruction from observational data, we first extract the streamfunction by vertically integrating the horizontal velocity. Then, inspired by the fact that the total dissipation rate is equal to the integral of the square of the vorticity, we approximate the vorticity using the negative square root of the dissipation-rate profile. We also substantially coarsen the computational data, using a vertical grid with spacing 0.01 that is about ten times larger than the grid spacing in the simulation. Figures (16–18) include the approximate streamfunction relations built in this fashion from two particular vertical cuts. The relations are reproduced qualitatively, if not quantitatively in all cases.

5.2. *A comparison with reality*

Guided by the considerations above, we examine some existing oceanographic and laboratory measurements of KHI, HWI and TCI in order to investigate the feasibility of distinguishing their respective nonlinear states using the functions $\mathcal{R}$ and $\mathcal{L}$. More specifically, KHI is distinguished by a monotonic $\mathcal{L}$ function in which $\mathcal{R}'$ plays little role with the density field acting almost like a passive tracer. HWI is distinguished by a three branch structure for $\mathcal{R}$ in which two of the branches share nearly the same value of ρ, and $\mathcal{L}$ has two branches away from the region associated with the vortex core. Finally, TCI inherently contains three layers in $\mathcal{R}$, and has a sharply peaked hump in $\mathcal{L}$, which is otherwise reasonably flat. Nevertheless, real evolving flows involve three-dimensional time-dependent dynamics on all scales down to the dissipation scales, which our nonlinear diagnostic is unlikely to capture in any detail. The most we may hope for is that the framework provides a 'flavor' of the associated nonlinear dynamics.

For KHI, we construct approximate streamfunction relations using oceanographic observations of a train of KH-like billows by van Haren *et al.* (2014); figure 19(a) shows the results, exploiting fits of their 1D data profiles. The details of the fits are provided in the appendix. A large-scale layering of the density field is evident in $\mathcal{R}$, and the functional form of $\mathcal{L}(\psi)$ is clearly of KH type. Note that a suitable choice for the phase speed of the observed structures is crucial in the construction; in producing figure 19(a), we adjusted the supposed phase speed to increase the degree of overlap between the two branches evident in $\mathcal{L}(\psi)$.

Figure 19 also plots approximate relationships for observations of HWI (Tedford *et al.* 2009) and TCI (Caulfield *et al.* 1995) from wave-tank experiments. The fits to the observed 1D profiles used for the constructions are again given in the appendix. For the data of Tedford *et al.* (2009), the three-branch structure of $\mathcal{R}$ is evident, as are the two distinct branches of $\mathcal{L}$ connected by a turning point at the minimum value of ψ. The form of $\mathcal{L}$ is much smoother here because the mean profiles provided do not contain much vertical structure. Nevertheless, both $\mathcal{R}$ and $\mathcal{L}$ are similar to the theoretical relations for HWI. For the data of Caulfield *et al.* (1995), we see a clear three-layer structure in $\mathcal{R}$, and a characteristic humped structure in $\mathcal{L}$, as expected for a nonlinearly saturated TCI.

6. Concluding remarks

We have performed a large number of 2D numerical simulations of the Taylor–Caulfield instability (TCI) which span the parameter space over which it arises in order to flesh out our knowledge of its nonlinear evolution. The simulations show a dichotomy between the behaviour at small or large bulk Richardson number J. For small J the billows formed by the saturation

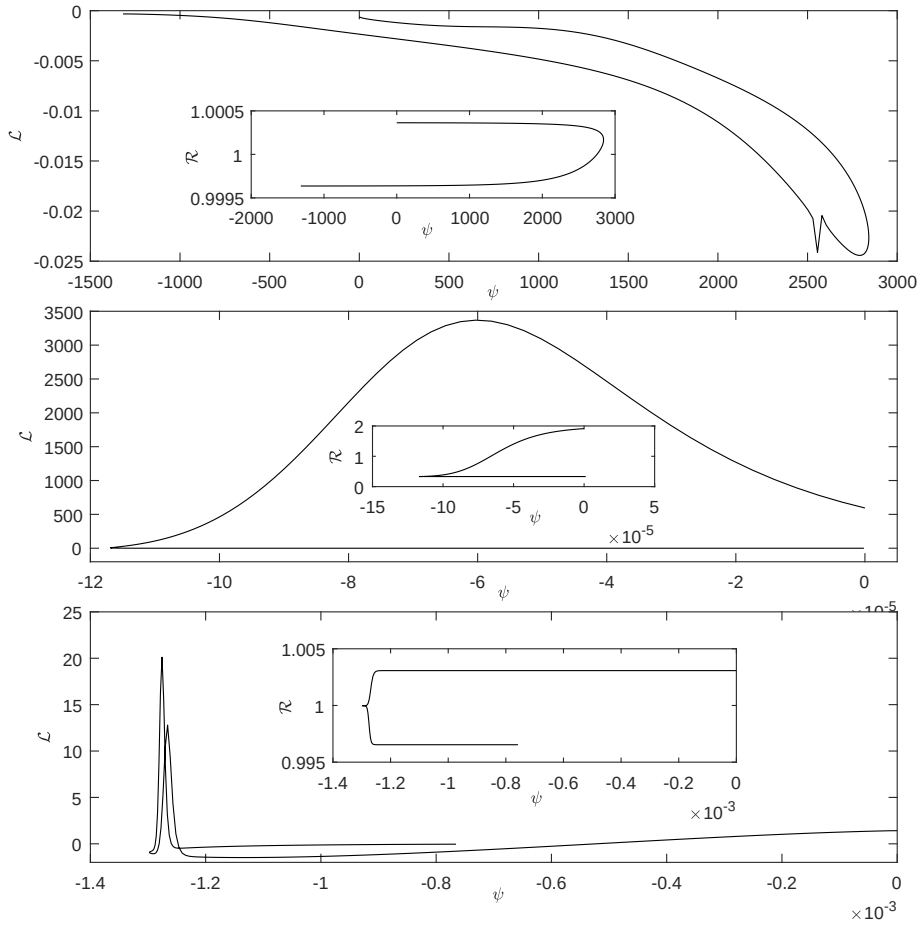

FIGURE 19. Approximations to the functional relationships $\mathcal{R}(\psi)$ and $\mathcal{L}(\psi)$ for approximated profiles taken from (a): the observational data of van Haren *et al.* (2014), and experimental data of (b): Tedford *et al.* (2009) and (c): Caulfield *et al.* (1995). Relations plotted for fits to the data; see appendix for details of the fits.

of the TCI modify the background flow to render the flow susceptible to further TCI, leading to an array of billows with cascading wavelength. At large J, large amplitude gravity waves on each density interface interact nonlinearly to produce significant horizontal density gradients and vorticity filaments. These new flow features very rapidly break down through small-scale KHI, generating a large amount of mixing. In addition, a previously observed late-time appearance of parasitic Holmboe waves is found for flows with sufficiently large Prandtl number.

Although our investigation has been primarily 2D, a limited investigation of the 3D behaviour of TCI at large k and J indicated that the break-down via small-scale KHI of nonlinear traveling waves is robust to weak noisy 3D perturbation. Nevertheless, further examination of TCI is needed in 3D in order to fully characterize its mixing characteristics and for the full range of secondary dynamics to be explored.

We have also provided two diagnostics to distinguish TCI from Kelvin–Helmholtz (KHI) and Holmboe-wave (HWI) instabilities. The first diagnostic is based on the properties of the linear normal modes and considers their conserved pseudomomentum. The second diagnostic applies

to the nonlinear steady states that can be found after the saturation of the linear instability and is based on the streamfunction relations characterizing steady nonlinear waves.

The pseudomomentum M of a linear disturbance must vanish exactly for an unstable normal mode and can be split into components stemming from the background vorticity and density gradients. This decomposition distinguishes the mechanisms exploited by the various kinds of flow instability and can be used to identify KHI, HWI or TCI for an arbitrary flow profile. This new classification is more robust than existing classification schemes since it follows directly from the conservation laws of the system.

The nonlinear diagnostic distinguishes the steady structures that appear after the saturation of the linear instability. We demonstrated the feasibility of applying this methodology to distinguish the three instabilities based only on 1D profiles of the data, as might be measured observationally or experimentally. Approximate relations found for observations of KHI in ocean currents, as well as experimental observations of HWI and TCI in wave tanks, revealed the same characteristic streamfunction relations as the 2D numerical simulations.

Appendix A

For the data of van Haren *et al.* (2014), we use the provided 1D profile of density ρ, and approximate the streamfunction via the North-South velocity V (in their notation) as $\psi \approx \int [V - V(-4450)]\mathrm{d}z$. We use the provided smooth profile of the gradient Richardson number $Ri(z) = N^2(z)/S^2(z)$, from which we back-out S^2 after calculating N^2 from ρ using $\rho_0 = 48.1275$ and then approximate the vorticity as $\zeta \approx -\sqrt{\epsilon} \approx -\sqrt{2S^2}$. Note that another approximation of the vorticity could be $\zeta \approx -V_z$ and that both of these estimates are rather crude. We chose to use the dissipation estimate since (at least in a global integral sense) it contains *all* contributions to the vorticity rather than that just due to one velocity component. To approximate their profiles, we use

$$V \approx 50\mathrm{sech}^2\left(\frac{z+4550}{120}\right) - 15, \tag{A 1}$$

$$Ri \approx 0.2 + 0.4\mathrm{sech}^2\left(\frac{z+4565}{20}\right) + 1.7\mathrm{sech}^2\left(\frac{z+4225}{20}\right) + 0.2\mathrm{sech}^2\left(\frac{z+4350}{50}\right), \tag{A 2}$$

$$\rho \approx 48.1275 - 0.0175\tanh\left(\frac{z+4425}{50}\right), \tag{A 3}$$

for vertical coordinate $z = -4650$ to -4225. To avoid an awkward issue of sign, we plot $\mathcal{L} = -\sqrt{2S^2} - (z+4400)N^2/\bar{V}$ in figure 19.

We approximate the profile of horizontal velocity and density of Tedford *et al.* (2009) as

$$u = 0.02\tanh[50(z-0.05)] - 0.005, \tag{A 4}$$

$$\rho = 1.4 - \tanh[300(z-0.055)], \tag{A 5}$$

for vertical coordinate $z = 0.05$ to 0.1. We approximate the streamfunction as $\psi \approx \int [u - \bar{u}]\mathrm{d}z$ where $\bar{u}$ is the mean of u, and the vorticity as $\zeta \approx -u_z$. We also set $\rho_0 = 1.205$. We plot $\mathcal{L} = \zeta - g(z - \bar{z})\mathrm{d}\rho/\mathrm{d}\psi/\rho_0$, where $\bar{z}$ is the z-location where $u(\bar{z}) = \bar{u}$.

The profile data of Caulfield *et al.* (1995) is approximated as

$$u = 0.045 - 0.055\mathrm{sech}^2[35(z-0.015)], \tag{A 6}$$

$$\rho = 1.0323 - \left(1.775\times10^{-3}\tanh[1000(z-0.058)] + 1.6\times10^{-3}\tanh[1000(z-0.043)]\right), \tag{A 7}$$

for vertical coordinate $z = 0$ to 0.1. We approximate the streamfunction as $\psi \approx \int [u - u(0.0505)]\mathrm{d}z$ and the vorticity as $\zeta \approx -u_z$. We also set $\rho_0 = 1.0325$. We plot $\mathcal{L} = \zeta - (g/\rho_0)(z - 0.0505)\mathrm{d}\rho/\mathrm{d}\psi$ to avoid issues of sign.

REFERENCES

Abarbanel, H. D. I., Holm, D. D., Marsden, J. E. & Ratiu, T. S. 1986 Nonlinear stability analysis of stratified fluid equilibria. *Phil. Trans. R. Soc. Lond. A* **318**, 349–409.

Balmforth, N. J., Roy, A. & Caulfield, C. P. 2012 Dynamics of vorticity defects in stratified shear flow. *J. Fluid Mech.* **694**, 292–331.

Bühler, Oliver 2014 *Waves and mean flows*. Cambridge University Press.

Carpenter, J. R., Balmforth, N. J. & Lawrence, G. A. 2010 Identifying unstable modes in stratified shear layers. *Phys. Fluids* **22**, 054104.

Carpenter, J. R., Tedford, E. W., Heifetz, E. & Lawrence, G. A. 2011 Instability in stratified shear flow: Review of a physical interpretation based on interacting waves. *Appl. Mech. Rev.* **64**, 060801.

Caulfield, C. P. & Peltier, W. R. 2000 The anatomy of the mixing transition in homogeneous and stratified free shear layers. *J. Fluid Mech.* **412**, 1–47.

Caulfield, C. P., Peltier, W. R., Yoshida, S. & Ohtani, M. 1995 An experimental investigation of the instability of a shear flow with multilayered density stratification. *Phys. Fluids* **7**, 3028–3041.

Eaves, T. S. & Caulfield, C. P. 2017 Multiple instability of layered stratified plane Couette flow. *J. Fluid Mech.* **813**, 250–278.

van Haren, H., Gostiaux, L., Morozov, E. & Tarakanov, R. 2014 Extremely long Kelvin–Helmholtz billow trains in the Romanche Fracture Zone. *Geophys. Res. Lett.* **41**, 8445–8451.

Helmholtz, H. 1868 On discontinuous movements of fluids. *Phil. Mag.* **36**, 337–346.

Holmboe, J. 1962 On the behavior of symmetric waves in stratified shear layers. *Geophys. Publ.* **24**, 67–113.

Howard, L. N. 1961 Note on a paper of John W. Miles. *J. Fluid Mech.* **10**, 509–512.

Kelvin 1871 Hydrokinteic solutions and observations. *Phil. Mag.* **42**, 362–377.

Lee, V. & Caulfield, C. P. 2001 Nonlinear evolution of a layered stratified shear flow. *Dyn. Atmos. Ocean.* **34**, 103–124.

Lindzen, R. S. & Barker, R. S. 1985 Instability and wave over-reflection in stably stratified shear flow. *J. Fluid Mech.* **151**, 189–217.

Long, R. R. 1953 Some aspects of the flow of stratified fluids I. A theoretical investigation. *Tellus* **5**, 42–57.

Mashayek, A., Caulfield, C. P. & Peltier, W. R. 2013 Time-dependent, non-monotonic mixing in stratified turbulent shear flows: implications for oceanographic estimates of buoyancy flux. *J. Fluid Mech.* **736**, 570–593.

Mashayek, A. & Peltier, W. R. 2012*a* The 'zoo' of secondary instabilities precursory to stratified shear flow transition. Part 1 Shear aligned convection, pairing, and braid instabilities. *J. Fluid Mech.* **708**, 5–44.

Mashayek, A. & Peltier, W. R. 2012*b* The 'zoo' of secondary instabilities precursory to stratified shear flow transition. Part 2 The influence of stratification. *J. Fluid Mech.* **708**, 45–70.

Mashayek, A. & Peltier, W. R. 2013 Shear-induced mixing in geophysical flows: does the route to turbulence matter to its efficiency? *J. Fluid Mech.* **725**, 216–261.

Miles, J. W. 1961 On the stability of heterogeneous shear flows. *J. Fluid Mech.* **10**, 496–508.

Peltier, W. R. & Caulfield, C. P. 2003 Mixing efficiency in stratified shear flows. *Annu. Rev. Fluid Mech.* **35** (1), 135–167.

Salehipour, H., Caulfield, C. P. & Peltier, C. P. 2016 Turbulent mixing due to the Holmboe wave instability at high reynolds number. *J. Fluid. Mech.* **803**, 591–621.

Scinocca, J. F. 1995 The mixing of mass and momentum by Kelvin–Helmholtz billows. *J. Atmos. Sci.* **52**, 2509–2530.

Smyth, W. D., Carpenter, J. R. & Lawrence, G. A. 2007 Mixing in symmetric Holmboe waves. *J. Phys. Oceanogr.* **37**, 1566–1583.

Smyth, W. D. & Winters, K. B. 2003 Turbulence and mixing in Holmboe waves. *J. Phys. Oceanogr.* **33**, 694–711.

Stuart, J. T. 1967 On finite amplitude oscillations in laminar mixing layers. *J. Fluid Mech.* **29**, 417–440.

Synge, J. L. 1933 The stability of heterogeneous liquid. *Trans. Roy. Soc. Can.* **27**, 1–18.

Taylor, G. I. 1931 Effect of variation in density on the stability of superposed streams of fluid. *Proc. R. Soc. Lond.* **132**, 449–523.

Taylor, J. R. 2008 Numerical simulations of the stratified oceanic bottom boundary layer. PhD thesis, Mech. Eng., UCSD.

Tedford, E. W., Pieters, R. & Lawrence, G. A. 2009 Symmetric Holmboe instabilities in a laboratory exchange flow. *J. Fluid Mech.* **636**, 137–153.